Electron beam shaping for actively outcoupling radiation from an x-ray regenerative amplifier free-electron laser

Jingyi Tang⦿,* Joseph P. Duris⦿,† Gabriel Marcus⦿, and Agostino Marinelli

SLAC National Accelerator Laboratory, Menlo Park, California 94025, USA

We present a method to actively outcouple radiation from an x-ray regenerative amplifier. The method uses an undulator within a cavity formed by the diamond mirror and is driven by a high repetition rate linac to build up a high power, narrow bandwidth seed within the cavity. Shaping the electron beam via laser heater modulation on a subsequent pass increases the bandwidth of the x-ray free-electron laser pulse beyond the bandwidth of the diamond mirrors, transmitting the radiation from the cavity. A fraction of the power from the shaped pulse is returned to the cavity, reducing the subsequent number of passes needed to rebuild the seed and increasing the duty factor. The cavity seeding may be used to produce short pulses that are significantly more stable than those produced via self-amplified spontaneous emission (SASE) or enhanced SASE.

I. INTRODUCTION AND MOTIVATION

X-ray free-electron lasers (FELs) are the brightest sources of x rays and have become valuable tools for the scientific community [1,2]. X-ray FELs typically employ self-amplified spontaneous emission (SASE), whereby shot noise within a high-brightness electron beam is amplified as it propagates through an undulator magnetic field [3,4]. The resulting radiation is composed of a chaotic series of many temporal modes due to the randomness of the shot noise seed, and the average coherence length and duration of these temporal modes are proportional to the gain length of the FEL. Self-seeding has been shown to increase the temporal coherence of FELs [5–8]. In a self-seeded FEL, the electron beam produces SASE radiation that is filtered and delayed by a narrow bandpass monochromator. The electron beam is correspondingly delayed by a magnetic chicane that washes out SASE-induced microbunching. The monochromatized radiation then interacts with the same delayed electron beam in a downstream seeded FEL amplifier stage, thereby producing a pulse with a temporal coherence set by the bandwidth of the monochromator. While the seed may be made significantly larger than the shot noise in the electron beam, its power is necessarily orders of magnitude below the FEL saturation power due to the spectral filter as well as the need to preserve the initial energy spread of the electron beam.

Cavity-based x-ray FELs such as x-ray FEL oscillators (XFELO) and regenerative amplifier FELs (RAFEL) [9,10] have been proposed to produce a single temporal mode over longtime scales. They offer the possibility of both high average and peak brightness x-ray beams that can be 2 to 3 orders of magnitude greater than conventional SASE FELs. Cavity-based FELs work by embedding an undulator within an x-ray optical cavity and returning a fraction of the radiation produced from one electron beam to seed the FEL instability for a following electron beam. Subsequent electron bunches may be delivered from the same rf waveform or produced by a high repetition rate linac such as the LCLS-II superconducting linac [11,12] or its planned high energy upgrade [13,14]. X-ray cavities typically employ crystals such as diamonds since they act as Bragg mirrors at x-ray wavelengths and exhibit high reflectivity within a narrow bandwidth depending on the radiation's incident angle [15]. Cavities with tunable photon energies may be made with a series of four crystals arranged in a geometry that maintains the cavity round trip time while tuning the Bragg angle [16]. The temporal coherence of the stored cavity radiation is largely determined by the inverse of the cavity bandwidth, and the properties of subsequent shots are more reproducible in comparison to the SASE [17]. Compared to self-seeded FELs, cavity-based x-ray FELs have a higher seed power, which can result in more efficient energy extraction if coupled with a strong undulator taper [18–21]. The power stored in the cavity can be outcoupled either actively [22,23] or passively [10,17,24–26].

In this work, we study the approach of outcoupling radiation from an x-ray regenerative amplifier FEL by

---

*jytang@slac.stanford.edu
†jduris@slac.stanford.edu

modulating the electron beam with a laser heater to broaden the bandwidth of the produced radiation beyond the cavity's acceptance. A strong narrow bandwidth x-ray seed is built up within a RAFEL after several passes using the standard electron beam properties delivered to a high-gain amplifier. A laser heater then imparts a controlled energy modulation onto a single electron bunch [27], which converts to a density modulation in the linac and compressors [28]. This density modulation drives space charge wakes which further modulates the energy of the electron beam by the time it enters the undulator, resulting in increased bandwidth of the produced radiation. The enhanced bandwidth radiation passes through the Bragg mirror immediately downstream of the undulator, releasing the radiation from the cavity. Only a small fraction of the enhanced bandwidth is returned by the cavity to seed subsequent passes. Pairing the electron bunch shaping technique with a strong and coherent cavity seed allows the FEL to quickly drive past saturation for the production of very high peak power pulses. However, the increased bandwidth necessarily shortens the produced radiation. Pulses comparable to a femtosecond or shorter may be useful for advanced imaging techniques (see, e.g., [29]). The stable and phase-locked short pulses can be useful in coherent nonlinear spectroscopy, which provides insight into the dynamics of molecules and materials with high temporal and spatial resolution [30–34].

The paper is organized as follows: Section II presents the x-ray RAFEL and cavity design parameters common to all simulation studies in the paper. Section III presents the cavity seed buildup and electron beam energy modulation to produce femtosecond pulses. Section IV shows simulations with the laser heater shaped to produce pairs of pulses with variable delay. In Sec. V, we present a two-stage tapered undulator within the cavity in conjunction with the laser heater shaping that results in sub-femtosecond pulses which compare favorably to sub-femtosecond pulses from simulations of an unseeded enhanced SASE (ESASE) FEL. A method of producing controllable trains of pulses is presented in Sec. VI. Finally, Sec. VII gives a discussion of the results of these simulations.

II. X-RAY RAFEL DESIGN

We base our pulse shaping study on the XRAFEL design being studied for producing nearly fully coherent hard x-ray pulses at an MHz repetition rate with the LCLS-II-HE high energy upgrade to the LCLS-II superconducting linac [13,14,17]. A diagram of the setup is shown in Fig. 1 and the parameters of the system are shown in Table I. An electron beam made with a longitudinally flattop laser pulse is produced from the LCLS-II photoinjector [35]. A laser heater is used to heat the electron beam to suppress the microbunching instability [27], and four linac sections and two bunch compressors accelerate and compress the beam to an energy of 8 GeV, a current of 1.6 kA, and an rms slice energy spread of 1 MeV. The electrons are then transported via a 2-km long transport line to the LCLS-II HXR planar undulators, each of which has 130 periods, each 26 mm long, and a peak undulator normalized strength variable up to $K = 2.44$ [36,37]. The undulators are centered between two mirrors, spaced 149 m apart in a $L_c = 300$ m long rectangular x-ray cavity (dimensions shown in Fig. 1) composed of four diamond mirrors oriented at 45° (400 Miller indices), resulting in a Bragg resonance of the mirrors centered at 9.8 keV.

The crystal thickness of 100 μm results in a peak reflectivity of nearly 100% and an FWHM reflective bandwidth of 78.5 meV [15]. Preliminary considerations of thermal loading effects on the cavity diamonds suggest only a small impact and will be the subject of future studies [38–40]. Two compound refractive lenses with a focal length of $f = L_c/8 = 37.5$ m placed equidistant both from each other and from the undulator establish a stable cavity transverse mode with a waist of 24.3 μm in the center of the undulator. We operate the cavity near the zero-detuning regime and the total slippage within the 40 m undulator is less than 1 fs which is far shorter than the seed electron beam duration. The undulators are tuned to an rms K of
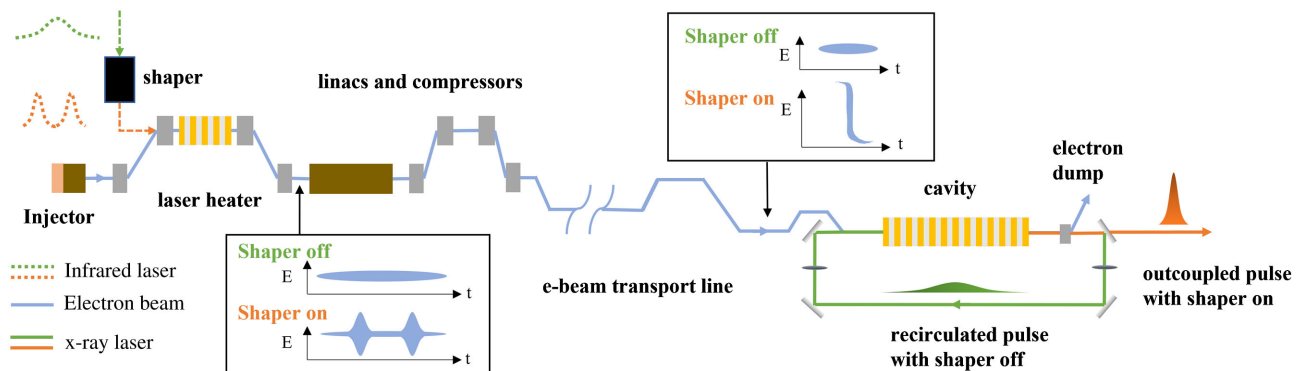

FIG. 1. Setup of electron beam shaping and radiation outcoupling from XRAFEL: laser heater, linacs and bunch compressor chicanes, long transport line, and cavity wrapped undulator line.

TABLE I.   LCLS-II-HE XRAFEL parameters common to all the simulations. Parameters after the $\pm$ symbol denote rms shot-to-shot variation in that parameter.

Electron beam at undulators	
Charge	100 pC
Energy	8 GeV $\pm$ 0.003% rms
Current	1.7 kA
Beam spacing (inverse repetition rate)	1 μs $\pm$ 5 fs rms
Transverse electron beam rms size	19.7, 21.0 μm
Electron beam rms duration	29.7 fs

Laser heater	
Electron beam energy	100 MeV
Undulator peak K	0.89
Undulator period	5.6 cm
Undulator length	51 cm
Laser wavelength	1021 nm
LH-induced energy spread	7.0 keV

Cavity	
Resonance	9.8 keV
FWHM bandwidth	88.9 meV
Cavity mode focus	Undulator center
Cavity mode waist	24.3 μm

FEL parameters	
Undulator K	1.169
Undulator period	26 mm
Periods per undulator	130
focusing-drift-defocusing-drift (FODO) period	7.8 m
Pierce parameter ρ	5.4×10^{-4}
3D gain length	4.36 m

1.169 and quadratically tapered to generate a strong seed. The FEL Pierce parameter and 3D power gain length are estimated to be 5.4×10^{-4} and 4.36 m, respectively, using an approximate FEL gain model [41]. The FEL resonant bandwidth is much larger than the cavity bandwidth so the FEL can support the amplification of radiation outside the cavity bandwidth. By using the laser heater to modulate the electron beam's energy, we can push, pull, or broaden the radiation's spectrum outside which is supported by the cavity. In this way, laser heater modulation of the electron beam offers a method of actively outcoupling radiation from the cavity.

All beam dynamics simulations presented are start-to-end simulations of the LCLS-II superconducting linac using ASTRA for the injector simulation [42], ELEGANT for particle tracking along the linac [43], and GENESIS for the FEL simulations [44]. Fresnel propagation is used to propagate the field in drift spaces between cavity optical components, each compound refractive lens is treated as a lossless parabolic phase mask in the transverse plane, and reflections and transmission for each mirror are modeled

using the dynamical theory of x-ray Bragg diffraction [15]. The energy and time of arrival of each electron bunch at the entrance of the undulator are determined randomly from normal distributions whose widths, shown in Table I, are chosen to model the expected bunch-to-bunch energy jitter of 0.003% and time of arrival jitter of 5 fs from the LCLS-II linac [45].

III. FEMTOSECOND PULSES

The production of femtosecond pulses begins with the generation of a strong seed within the cavity using the nominal unshaped 30-fs low energy spread electron beam. Figures 2(a) and 2(b) show the longitudinal phase spaces of this electron beam after the laser heater and at the entrance of the undulators. In this case, a long laser heater pulse uniformly heats the slice energy spread of the electron beam to 7.0 keV in order to suppress the microbunching instability in the linac, bunch compressors, and transport to the undulators. The 3rd through 11th undulators are quadratically tapered to reduce the undulator parameter K by 1.4% over 35 m [see Fig. 3(a)] to enhance the power extracted from the shaped electron beam. With each pass, a fraction of the produced radiation is returned via the cavity optics to the entrance of the undulator, and the intracavity peak power builds up from shot noise to about 10 GW after the undulator and the power returned to the undulator entrance via the cavity is 2 GW in the steady state after 15 passes, as shown in Fig. 3(b). Figure 3(c) shows the power profile of the radiation at the end of the undulator and the seed pulse returned to the undulator in the steady state, which has an FWHM duration of 55 fs, a peak power of 2 GW, and an FWHM bandwidth of 50 meV. Figure 3(d) shows the spectrum of the postundulator radiation, which is
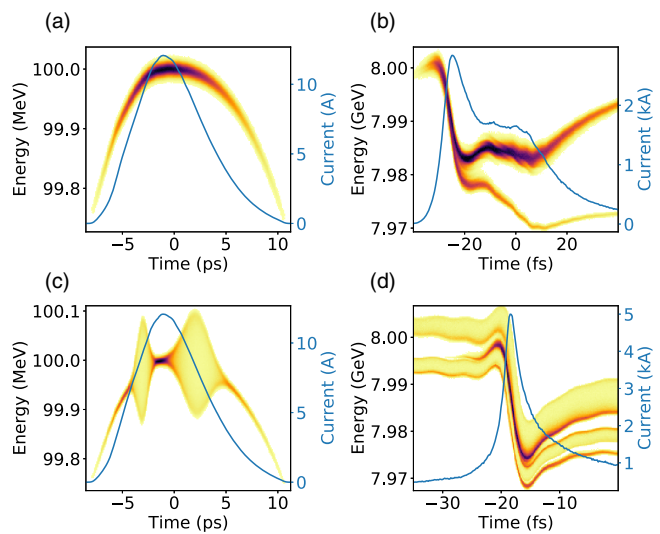

FIG. 2.   Longitudinal phase space after the laser heater (a, c) and right before the hard x-ray undulator line (b, d) for the seed (a, b) and shaped (c, d) beams.
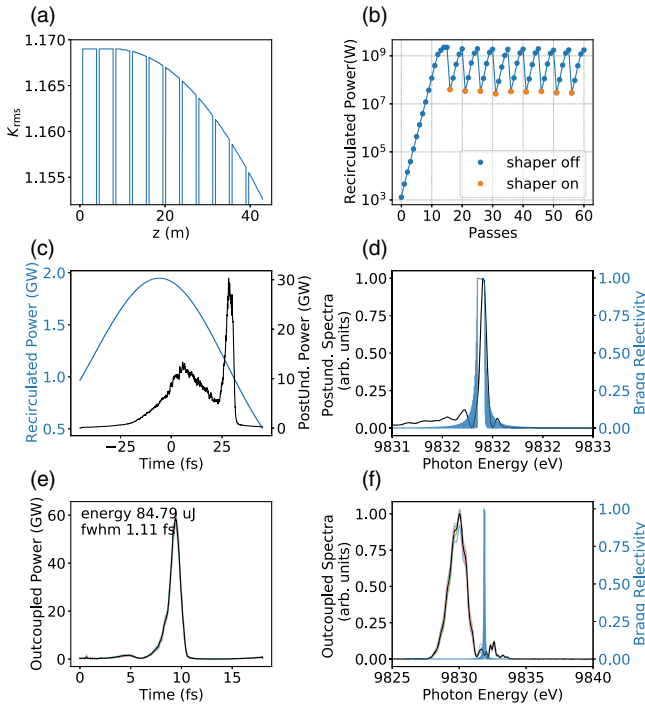
FIG. 3. Femtosecond pulses outcoupling. Undulator taper configuration (a), recirculated peak power for each iteration (b). Here the orange dots represent the shots when the shaping laser is on. Power profile after the undulator (black) and recirculated radiation profile (blue) from seed beam (c), a spectrum of the radiation after the undulator (d), 10 shots of outcoupled radiation from the shaped beam (e) and their spectrum (f), with colored lines for each shot and a black line for the average. Bragg reflectivity as a function of photon energy is shown by the blue line in (d) and (f).

broader than the Bragg reflection bandwidth mainly due to the horn in the head of the seed beam. As a result, for the unshaped e-beam, about 40% of the pulse energy is reflected and recirculated.

Once the cavity power has built up to a steady state, the shaping laser is switched on for one shot, providing a time-dependent slice energy spread modulation, as shown in Fig. 2(c). Two Gaussian pulses with FWHM widths of 1.2 and 2.8 ps spaced 5.1 ps apart heat all but a roughly 1-ps region of the beam in the core of the distribution to keep it from lasing downstream. The cold beam region is compressed by a factor of 160 while it undergoes acceleration and compression in the LCLS-II linac. This results in a distribution dominated by a prominent 5-fs current spike at the entrance to the hard x-ray undulator. Additionally, the regions heated by the shaping laser are strongly dispersed by the significant R_{56} of the bunch compressors, as shown in Fig. 2(d).

The correlated energy spread of the short, shaped beam is enhanced by the longitudinal space charge force in the 2-km bypass line from the linac to the undulators.

The shaped electron beam and the steady-state x-ray seed pulse enter the same undulator line, producing a femtosecond duration pulse with peak power and spectral bandwidth significantly increased relative to their unshaped counterparts. This enhancement in the x-ray power and bandwidth and a sharp reduction in the pulse duration are direct results of the effect of laser-induced shaping on the current and energy profile of the electron beam. Specifically, the presence of a high current region enhances the gain within the short spike, while the large energy chirp reduces the gain outside of the spike in a similar way to femtosecond slicing of a chirped electron beam with a narrow bandwidth seed [46,47]. Thus the pulse duration is decreased by the electron beam energy chirp and enhanced current. The first cavity mirror transmits the shaped pulse with modest attenuation as its bandwidth far exceeds the reflective bandwidth of the mirror. The transmitted pulse, shown in Figs. 3(c) and 3(d), has a peak power of nearly 40 GW, an FWHM duration of 1.3 fs, and an FWHM spectral bandwidth of nearly 2 eV. If we define an effective XRAFEL quality factor $Q = 2\pi U_s / U_l$ where U_s is energy stored and U_l is energy lost, then with e-beam shaper off, at steady state $Q = 6.7$ and with e-beam shaper on, $Q = 0.14$. This shows that changing the gain in this scheme is similar to Q-switching in an optical cavity; however, in this scheme, we are changing the gain medium and radiation bandwidth rather than the cavity acceptance.

The pulse reflected from the cavity mirrors has a peak power of more than 10^7 Watts and is returned to the undulator to seed subsequent passes. While the peak power is about 2 orders of magnitude below the steady-state seed power of 2 GW, it exceeds the shot noise power by several orders of magnitude, reducing the number of passes needed to build up the steady-state seed again. After four passes, the seed power again reaches 2 GW and the shaping laser can be switched on to produce another short pulse. In this way, the duty cycle can be increased from 1 in 17 shots to 1 in 5 shots.

The space charge–induced electron beam energy chirp also provides an opportunity to control the pulse duration of the shaped pulse. Nearly all of the space charge–induced chirp is acquired in the accelerator and long transport line before the dogleg. Therefore, the duration of the current spike may be linearly controlled via R_{56} near the end of the beamline. The R_{56} of the last dogleg before the undulator line, named DL2, can be manipulated by adjusting two skew quadrupoles and a series of stronger quadrupoles in the dispersive region of the dogleg to change the R_{56} while keeping the dispersion fixed [48]. The maximum change to the DL2 R_{56} is limited by the skew quadrupoles' power supplies to about ± 300 μm, where we use the convention that a free-space drift has $R_{56} < 0$ and anomalous R_{56} takes positive values. Figure 4 shows the longitudinal phase spaces and current profiles at the undulator entrance for three different relative DL2 R_{56} values. The beam energy chirp entering this region is about 25 MeV in 3 fs so
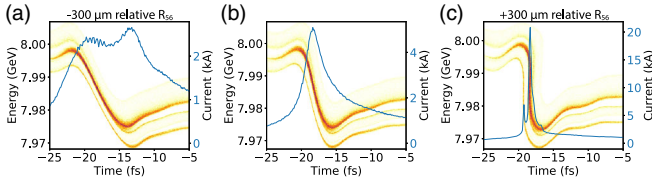
FIG. 4. The electron beam's current profile can be controlled by varying the R_{56} of DL2, the last dogleg before the undulator line. (a) (b) and (c) show the longitudinal phase space of electron beam at the start of hard x-ray undulator line with $-300\ \mu\mathrm{m}$, $0\ \mu\mathrm{m}$, and $+300\ \mu\mathrm{m}$ DL2 R_{56} respectively.

subtracting $300\ \mu\mathrm{m}$ R_{56} halves the chirp [see Fig. 4(a)], whereas adding that amount of R_{56} is enough to fully compress the chirp [Fig. 4(c)].

The outcoupled power profiles of steady-state seeded FEL simulations with these beams are shown in Fig. 5(a). The pulse duration varies linearly with respect to the relative R_{56} [Fig. 5(b)]. On the other hand, the pulse energy increases a modest 36%, whereas the peak power increases 9.2 times [Fig. 5(c)]. This increase in power is accompanied by a similar 8.8 times increase in spectral bandwidth [Fig. 5(d)]. In this way, the pulse duration of the outcoupled pulse may be controlled via R_{56}. It is important to note that the change of the transport R_{56} is also applied to the unshaped electron beam used to generate the steady-state cavity seed [see Fig. 2(b)]; however, the seed beam is unperturbed as the core of the beam used to generate the seed has very little correlated energy spread.

Alternatively, the current spike duration can be controlled independent of R_{56} by adding a low power baseline laser heater pulse to the high-power shaped pulse. This increases the slice energy spread after the laser heater, elongating the beam in the second bunch compressor and
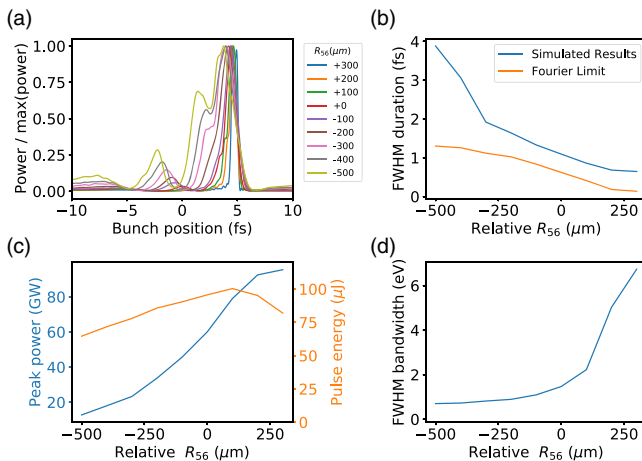

FIG. 6. Longitudinal phase space of electron beam after BC2 (a,c,e) and the start of hard undulator line (b,d,f) with different nominal laser heater–induced energy spreads specified above (a, c,e) relative to the beam energy in the laser heater.

reducing the spike's space charge–induced chirp at the undulator entrance, as shown in Fig. 6. Having two independent ways to control the pulse duration will prove useful for selectively shaping pairs of pulses in the following section.

IV. PAIRS OF PULSES

Heating all but a short region of electron beam results in a shortened x-ray pulse with enhanced bandwidth enabling cavity outcoupling. Gating the heater laser to produce two such cold beams may result in pairs of such femtosecond pulses. This is illustrated in Fig. 7, which shows that current spikes with different delays can be generated by controlling the spacing and duration of three Gaussian shaping lasers. The laser parameters of each case are listed in Table II.

FIG. 5. Outcoupled x-ray FEL pulse duration vs relative change to DL2 R_{56}. Outcoupled power profiles (a) show a linearly shrinking pulse duration (b) without significantly changing the overall pulse energy (c). The pulse bandwidth (d) significantly exceeds the reflective bandwidth of the mirrors for each shot.
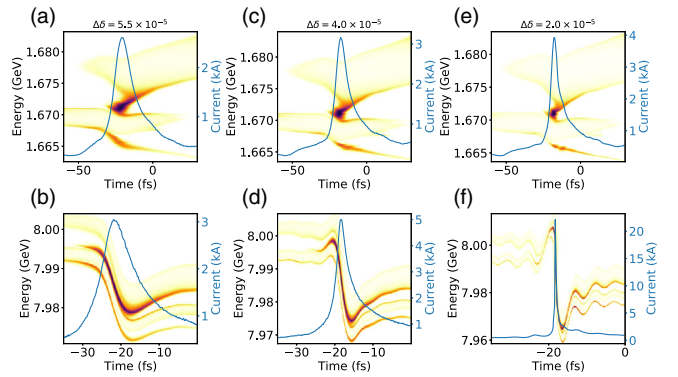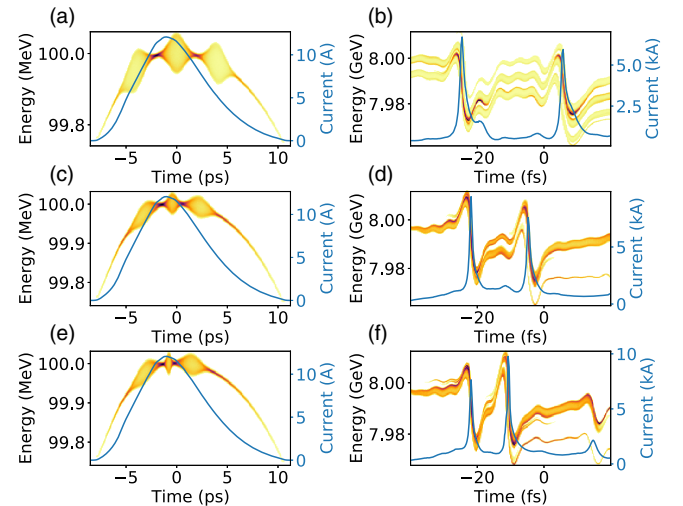

FIG. 7. Longitudinal phase space after the laser heater (a, c, e) and right before the hard x-ray undulator line (b, d, f) for shaped beams with two current spikes. The delay time between the two spikes are 31.0 fs (a, b), 17.3 fs (c, d), and 9.5 fs (e, f) respectively.

TABLE II.   Laser parameters for pulse pair simulations.

Laser heater	
Final delay time (fs)	11.3
Laser waist (μm)	500
Peak power (MW)	0.8, 0.8, 0.8
FWHM (ps)	1.9, 0.47, 1.9
Spacing between pulses (ps)	2.3, 2.3
Final delay time (fs)	17.4
Laser waist (μm)	500
Peak power (MW)	0.8, 0.8, 0.8
FWHM (ps)	1.9, 0.9, 1.9
Spacing between pulses (ps)	2.8, 2.7
Final delay time (fs)	31.0
Laser waist (μm)	500
Peak power (MW)	2.0, 2.0, 2.0
FWHM (ps)	1.8, 1.8, 1.8
Spacing between pulses (ps)	4.0, 4.0

The duration of both current spikes and subsequent FEL pulses can be controlled at the same time by varying the dogleg R_{56} to control the compression of each energy-chirped current spike as demonstrated before in Figs. 4 and 5. Since the space charge–induced energy chirp of each current spike is similar, each current spike and subsequent FEL pulses respond similarly so that the duration of each pulse is nearly identical.

Alternatively, the duration of each current spike and subsequent FEL pulse can be individually controlled by
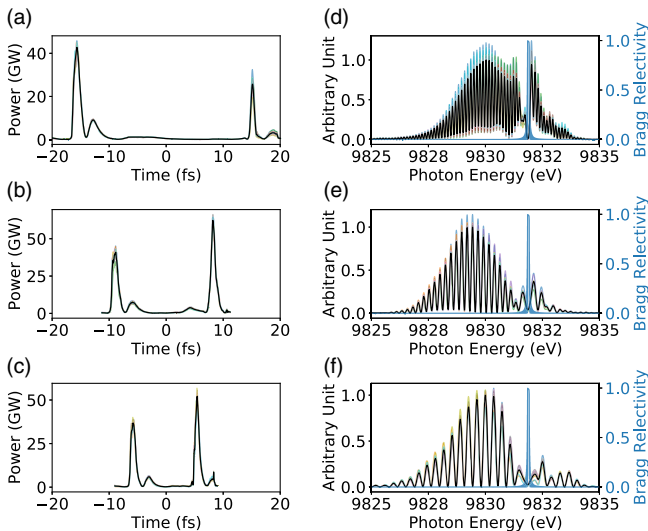

FIG. 8. Pulse pairs outcoupling. Ten shots of outcoupled radiation from shaped beam (a–c) and their spectrum (d–f), with delay time at 9.5 fs (a,d) 17.3 fs (b,e), and 31.0 fs (c, f) respectively. The colored line for each shot and the black line for the average. Bragg reflectivity, as a function of photon energy, is shown by the blue dash line in (d–f).
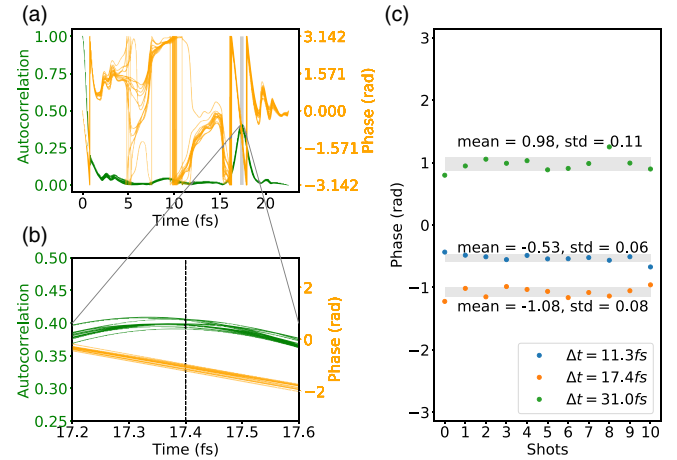

FIG. 9.   Analysis of phase jitter is shown at a fixed delay between two pulses in the pulse pair. (a) The amplitude (green line) and phase (yellow line) of the autocorrelation are shown for the on-axis pulse pair radiation field with 17.3-fs delay, and (b) an enlarged view shows the correlation and relative phase between the pairs of pulses. (c) The relative phase between the pulse pairs is shown for 11 shots at delay times of 9.5 fs (blue), 17.3 fs (yellow), and 31.0 fs (green).

using a short laser centered on only one gated region of the electron beam to control the slice energy spread and space charge–induced chirp of a single spike, as shown in Fig. 6. The combination of these two knobs, dogleg R_{56} and slice energy spread, allows tailoring each pulse individually for pump-probe experiments.

The power profile and spectrum of the outcoupled radiation are shown in Fig. 8, where the colored lines show different shots and the black line shows the average. The stable interference pattern in the spectrum indicates good coherence between the two pulses.

We analyzed the correlation and phase jitter of the two pulses in the pulse pair by computing the autocorrelation of the on-axis radiation field, as shown in Fig. 9. Auto-correlation is the cross-correlation of the field with a delayed copy of itself as a function of delay, the amplitude of which is normalized to unity at zero delay. A peak at 17.4 fs in Figs. 9(a) and 9(b) indicates a strong correlation between the pulse pair. Maximum amplitude of 0.5 would be reached given the autocorrelation normalization if the two pulses in the pair were identical. Here we have the maximum correlation of about 0.4, which indicates decent coherence between the pulse pairs. Furthermore, the relative phase difference between the pulse pair can be determined from the complex autocorrelation. In Fig. 9(c), we computed the phase difference at each shot for three sets of pulse pairs at various fixed delays, and the statistics show that from shot to shot, these pulse pairs are phase locked to within a couple of hundred milliradians. Such phase-locked pulse pairs may be useful for coherent pump-probe experiments.
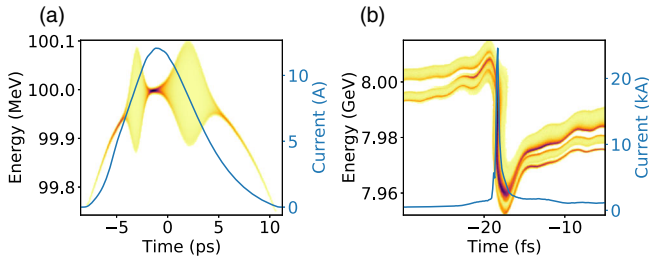
FIG. 10.   (a) The same two laser pulses, as in Fig. 2, heats all but a 2-ps slice of the electron beam after the laser heater, but the baseline laser heater–induced energy spread for the cold core beamlet is reduced to 2 keV rms. (b) The longitudinal phase space right before the undulators shows a 20 kA, 0.2-fs short current spike.

V. SUB-FEMTOSECOND PULSES

Section III details the generation and duration control of femtosecond pulses, whereby two NIR laser pulses in a laser heater gate a short duration of high-brightness electron beam and a third, longer NIR laser pulse controls the nominal slice energy spread of that electron beam. Removing the long NIR laser pulse maximizes the brightness of the short, gated electron beam, enabling maximum compression. Figure 10(b) shows such a configuration resulting in a short 0.2-fs current spike with a linear chirp of about 100 MeV/fs. The enhanced current of the short spike reduces the power gain length and coherence length to support shorter pulses. Linearly tapering the undulators to match the FEL resonant energy gradient with the electron beam chirp further reduces the gain length to generate higher power, shorter pulses.

Figure 11(a) shows the normalized field strength K_{rms} along the undulator line in a scenario where the last six undulators are used to build up the seed in passes with an unshaped electron beam. The first two of these undulators have constant magnetic field strength to establish bunching from the steady-state seed, whereas the last four undulators are quadratically tapered to enhance energy extraction. The seed power builds up after 10 passes with the unshaped beam, as shown in Fig. 11(b).

After the seed power has built up, the shaping laser is switched on to shape the electron beam as in Fig. 10(b). Another set of undulators positioned just before the six seed undulators is tuned to have a linearly increasing magnetic field to match the linear energy chirp of the shaped beam. The strong reverse taper ensures that this short pulse undulator section only couples to the shaped electron beam and does not affect the unshaped electron beam during the seed buildup. Conversely, the resonant energy of the seed taper is sufficiently detuned from the lasing part of the shaped electron beam (by 30 eV) to not affect the short pulse. The resulting shaped FEL pulse extracted from the cavity has an FWHM pulse duration of 0.1 fs, an energy of 21 μJ, and an FWHM bandwidth of 20 eV [see Figs. 10(c) and 10(d)]. Although most of the power is outcoupled from the cavity, 100s of kW are returned to the undulator which restarts the seed growth process with the unshaped electron beam. After 10 passes, the seed power has grown back to its steady-state value of a couple of GW so the shaping laser can be switched on every 5 passes to generate attosecond x-ray pulses at 100 kHz.

The stability of these pulses from the cavity seeding is evident from the low amount of variation in the power profiles of 35 shots shown in Fig. 11. Figure 12 shows that the stability of these pulses compares favorably to standard ESASE lasing. The blue histograms show the distributions of properties of 35 cavity-seeded x-ray FEL pulses. The orange histograms show the distributions for 35 pulses
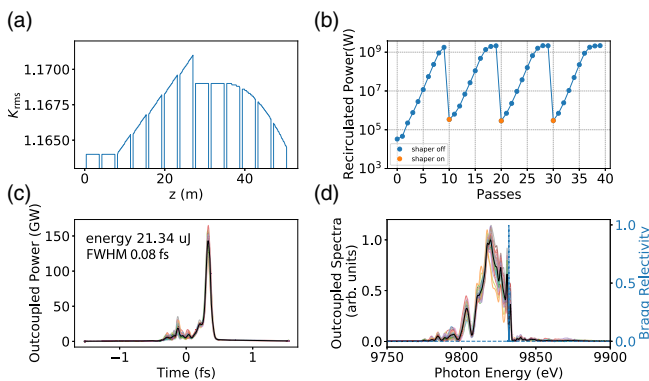

FIG. 11.   Attosecond pulses outcoupling. Undulator taper configuration (a), recirculated peak power for each iteration (b). Here the orange dots represent the shots when the shaper is on. Thirty-five shots of outcoupled radiation from the shaped beam (c) and their spectrum (d), with the colored line for each shot and black line for the average. Bragg reflectivity, as a function of photon energy, is shown by the blue dash line in (d).
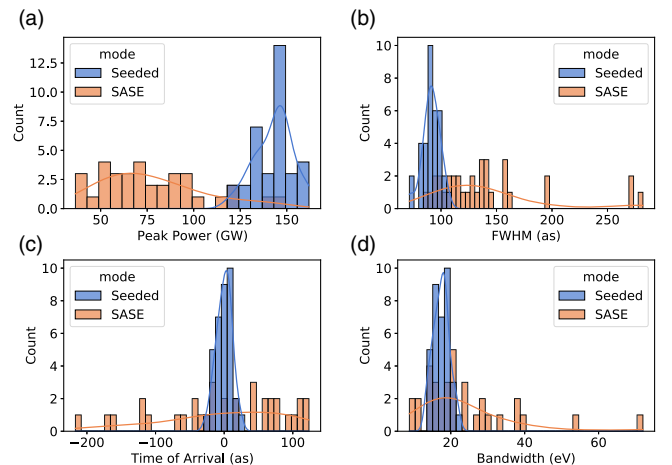

FIG. 12.   Comparison of stability between ESASE and seeded attosecond pulses' properties: the histogram of 30 shots for x-ray peak power (a), full-width half-maximum pulse duration (b), time of arrival (c), and spectral bandwidth (d) from SASE (orange) and seeded mode (blue), respectively.

produced using the same shaped electron beam but without seeding. For this ESASE data set, the lack of a strong seed necessitated elongating slightly the reverse taper to maximize the peak power.

The cavity-seeded short pulses have significantly more stable peak power, pulse duration, bandwidth, and time of arrival. Pairs of such pulses may be made as before by stacking three shaped pulses but without a long duration baseline heating pulse, resulting in phase stable pairs of attosecond pulses. Alternatively, by selectively heating just one of the sliced bunches within the shaped electron beam as in Fig. 5, an attosecond and femtosecond pulse may be generated in the same shot.

VI. TRAINS OF PULSES

Trains of pulses can be produced by generating a periodic gate by stacking two linearly chirped laser pulses with a delay [49]. The electric field for a linearly chirped Gaussian pulse with FWHM duration Δt and bandwidth $\Delta \omega$ at a time t is given by

$$E = E_0 \exp\left(-i(\phi + t\omega_0 + t^2\omega_1/2) - 2t^2 \ln 2/\Delta t^2\right), \quad (1)$$

where ϕ is a constant phase, ω_0 is the frequency, and the amplitude of the electric field is given by $E_0 = \sqrt{2Z_0 P_0/\pi w_0^2}$ where Z_0 is the impedance of free space, P_0 is the peak power, and w_0 is the waist or twice the rms transverse width. The linear chirp parameter is given by $\omega_1 = \pm\sqrt{\Delta\omega^2/\Delta t^2 - 16 \ln 2/\Delta t^4}$ where the sign of the parameter reflects the sign of the chirp. Adding two copies of this field with a time delay δt results in a pulse with an envelope modulated by a temporal comb with constant frequency and nodes separated by $T = 2\pi/\delta t\omega_1$. Figure 13 shows an example power profile with two stacked pulses as well as the node separation in time.

Application of this laser pulse to the electron beam in the laser heater results in a train of short beamlets, each of which are accelerated and compressed to produce a train of high current spikes, as shown in Figs. 14(a) and 14(b).
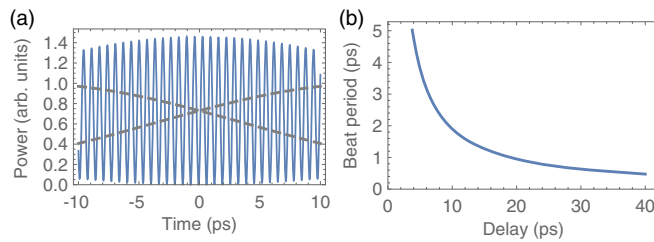
FIG. 13. (a) Laser power profile for two copies of a linearly chirped Gaussian pulse with 43-ps FWHM duration, wavelength of 1030 nm, and FWHM bandwidth of 8 nm, with 29-ps delay between pulses. The dashed lines show the power profiles if one of the pulses was blocked. (b) The node spacing decreases with increasing pulse separation.
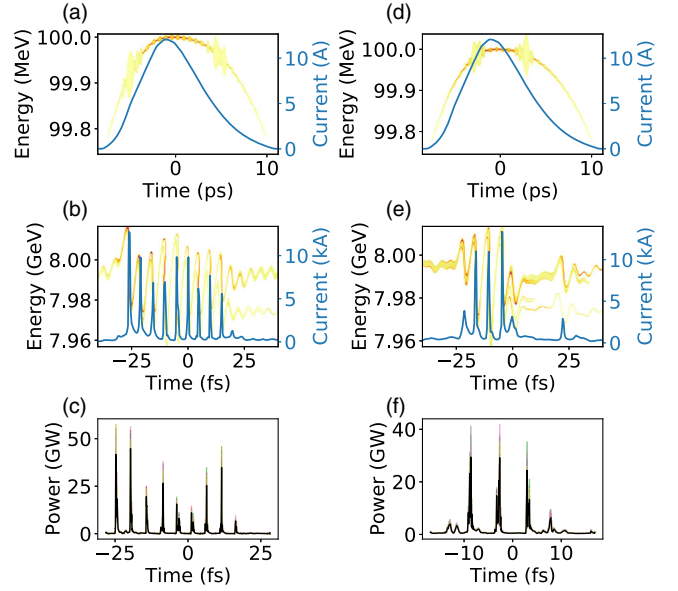
FIG. 14. Longitudinal phase space of the e-beam after the laser heater (a) and right before the hard x-ray undulator line (b) to generate attosecond x-ray pulse train (c) by stacking two linearly chirped laser pulses with FWHM 43 ps and relative delay 29 ps. An additional pair of laser pulses (FWHM 1 ps, delay 5.3 ps) is used to gate the pulse train and control the number of pulses in the train (d and e).

Applying the same undulator line used for generating attosecond pulses [Fig. 11(a)] results in a train of femtosecond pulses shown in Fig. 14(c). As with the pulse pair case shown earlier, the cavity seed ensures that each pulse in the train has a fixed phase relationship to the other pulses.

The properties of the x-ray pulse train may be changed by tailoring the laser heater shaping laser. Varying the period of the laser beat wave changes the interpulse spacing in the x-ray pulse train, whereas varying the baseline laser heater power or beamline R_{56} elongates the duration of each pulse in the train. Combining the beat wave laser profile with a baseline laser heater with a linearly increasing power profile results in a pulse train with increasing or decreasing duration pulses within the train. Furthermore, adding another pair of laser pulses in the laser heater at the edges of the electron beam gates the train envelope [Figs. 14(d) and 14(e)] controlling the x-ray pulse train envelope duration, as shown in Fig. 14(f). In this way, the beat wave laser makes a train of short beamlets, each of which gain correlated energy spread from longitudinal space charge which broadens the FEL beyond the cavity bandwidth to outcouple radiation, while a long baseline laser and another pair of laser pulses control the properties of the x-ray pulse train.

VII. DISCUSSION

In this paper, we have shown an approach to outcoupling radiation from an x-ray cavity in a regenerative amplifier

x-ray free-electron laser. Isolated or phase-stable pairs of x-ray pulses may be produced at high rates and the duration of each pulse may be varied from several femtoseconds to as short as 100 attoseconds by controlling the beamline's longitudinal dispersion or the slice energy spread of each cold electron beamlet. The cavity seed significantly increases the stability of the output pulses compared to SASE. Interfering two copies of a linearly stretched laser pulse in the laser heater results in a coherent train of pulses, each with controllable durations, and the overall train length can be controlled by gating with another two laser pulses. These results offer a path toward coherent control of hard x-ray FELs at high repetition rate machines such as European XFEL and the LCLS-II superconducting linac.

ACKNOWLEDGMENTS

———

[1] C. Bostedt, S. Boutet, D. M. Fritz, Z. Huang, H. J. Lee, H. T. Lemke, A. Robert, W. F. Schlotter, J. J. Turner, and G. J. Williams, Linac coherent light source: The first five years, Rev. Mod. Phys. 88, 015007 (2016).

[2] J. Rossbach, J. R. Schneider, and W. Wurth, 10 years of pioneering x-ray science at the free-electron laser flash at DESY, Phys. Rep. 808, 1 (2019).

[3] R. Bonifacio, C. Pellegrini, and L. Narducci, Collective instabilities and high-gain regime in a free electron laser, Opt. Commun. 50, 373 (1984).

[4] A. Kondratenko and E. Saldin, Generating of coherent radiation by a relativistic electron beam in an ondulator, Part. Accel. 10, 207 (1980).

[5] G. Geloni, V. Kocharyan, and E. Saldin, A novel self-seeding scheme for hard x-ray FELs, J. Mod. Opt. 58, 1391 (2011).

[6] J. Amann, W. Berg, V. Blank, F.-J. Decker, Y. Ding, P. Emma, Y. Feng, J. Frisch, D. Fritz, J. Hastings et al., Demonstration of self-seeding in a hard-x-ray free-electron laser, Nat. Photonics 6, 693 (2012).

[7] I. Inoue, T. Osaka, T. Hara, T. Tanaka, T. Inagaki, T. Fukui, S. Goto, Y. Inubushi, H. Kimura, R. Kinjo et al., Generation of narrow-band x-ray free-electron laser via reflection self-seeding, Nat. Photonics 13, 319 (2019).

[8] I. Nam, C.-K. Min, B. Oh, G. Kim, D. Na, Y. J. Suh, H. Yang, M. H. Cho, C. Kim, M.-J. Kim et al., High-brightness self-seeded x-ray free-electron laser covering the 3.5 kev to 14.6 kev range, Nat. Photonics 15, 435 (2021).

[9] K.-J. Kim, Y. Shvyd'ko, and S. Reiche, A Proposal for an X-Ray Free-Electron Laser Oscillator with an Energy-Recovery Linac, Phys. Rev. Lett. 100, 244802 (2008).

[10] Z. Huang and R. D. Ruth, Fully Coherent X-Ray Pulses from a Regenerative-Amplifier Free-Electron Laser, Phys. Rev. Lett. 96, 144801 (2006).

[11] T. O. Raubenheimer, LCLS-II conceptual design report, SLAC National Accelerator Laboratory, CA, Technical Report SLAC-R-978, 2015.

[12] T. Raubenheimer, Technical Challenges of the LCLS-II, in Proceedings of the 6th International Particle Accelerator Conference, IPAC'15, Richmond, VA, 2015 (JACoW, Geneva, Switzerland).

[13] T. O. Raubenheimer, LCLS-II HE conceptual design report, SLAC National Accelerator Laboratory, CA, Technical Report SLAC-R-1098, 2018.

[14] T. Raubenheimer, The LCLS-II-HE, A high energy upgrade of the LCLS-II, in Proceedings of the 60th ICFA Advanced Beam Dynamics Workshop, FLS'18, Shanghai, China, 2018 (JACoW Publishing, Geneva, Switzerland, 2018).

[15] Y. Shvyd'ko and R. Lindberg, Spatiotemporal response of crystals in x-ray Bragg diffraction, Phys. Rev. ST Accel. Beams 15, 100702 (2012).

[16] K.-J. Kim and Y. V. Shvyd'ko, Tunable optical cavity for an x-ray free-electron-laser oscillator, Phys. Rev. ST Accel. Beams 12, 030703 (2009).

[17] G. Marcus, A. Halavanau, Z. Huang, J. Krzywinski, J. MacArthur, R. Margraf, T. Raubenheimer, and D. Zhu, Refractive Guide Switching a Regenerative Amplifier Free-Electron Laser for High Peak and Average Power Hard X Rays, Phys. Rev. Lett. 125, 254801 (2020).

[18] Y. Jiao, J. Wu, Y. Cai, A. W. Chao, W. M. Fawley, J. Frisch, Z. Huang, H.-D. Nuhn, C. Pellegrini, and S. Reiche, Modeling and multidimensional optimization of a tapered free electron laser, Phys. Rev. ST Accel. Beams 15, 050704 (2012).

[19] C. Emma, J. Wu, K. Fang, S. Chen, S. Serkez, and C. Pellegrini, Terawatt x-ray free-electron-laser optimization by transverse electron distribution shaping, Phys. Rev. ST Accel. Beams, 17, 110701 (2014).

[20] J. Duris, A. Murokh, and P. Musumeci, Tapering enhanced stimulated superradiant amplification, New J. Phys. 17, 063036 (2015).

[21] J. Duris, P. Musumeci, N. Sudar, A. Murokh, and A. Gover, Tapering enhanced stimulated superradiant oscillator, Phys. Rev. Accel. Beams 21, 080705 (2018).

[22] P. Bucksbaum and R. Merlin, The phonon Bragg switch: A proposal to generate sub-picosecond x-ray pulses, Solid State Commun. 111, 535 (1999).

[23] J. Krzywiński, Y. Feng, A. Halavanau, Z. Huang, A. Kiss, J. MacArthur, G. Marcus, T. Sato, and D. Zhu, Q-switching of x-ray optical cavities by using boron doped buried layer under a surface of a diamond crystal, in Proceedings of 39th International Free Electron Laser Conference, FEL'19, Hamburg, Germany, 2019 (JACoW Publishing, Geneva, Switzerland, 2019), paper TUP033, pp. 122–125.

[24] J. P. MacArthur, A. A. Lutman, J. Krzywinski, and Z. Huang, Microbunch Rotation and Coherent Undulator Radiation from a Kicked Electron Beam, Phys. Rev. X 8, 041036 (2018).

[25] H. P. Freund, P. Van der Slot, and Y. Shvyd'ko, An x-ray regenerative amplifier free-electron laser using diamond pinhole mirrors, New J. Phys. 21, 093028 (2019).

[26] Y. Shvyd'ko, Output coupling from x-ray free-electron laser cavities with intracavity beam splitters, Phys. Rev. Accel. Beams **22,** 100703, 2019.

[27] Z. Huang *et al.*, Measurements of the linac coherent light source laser heater and its impact on the x-ray free-electron laser performance, Phys. Rev. ST Accel. Beams **13,** 020703 (2010).

[28] D. Cesar, A. Anakru, S. Carbajo, J. Duris, P. Franz, S. Li, N. Sudar, Z. Zhang, and A. Marinelli, Electron beam shaping via laser heater temporal shaping, Phys. Rev. Accel. Beams **24,** 110703 (2021).

[29] D. Rupp, L. Flückiger, M. Adolph, A. Colombo, T. Gorkhover, M. Harmand, M. Krikunova, J. P. Müller, T. Oelze, Y. Ovcharenko, M. Richter, M. Sauppe, S. Schorb, R. Treusch, D. Wolter, C. Bostedt, and T. Möller, Imaging plasma formation in isolated nanoparticles with ultrafast resonant scattering, Struct. Dyn. **7,** 034303 (2020).

[30] W. Min, C. W. Freudiger, S. Lu, and X. S. Xie, Coherent nonlinear optical imaging: Beyond fluorescence microscopy, Annu. Rev. Phys. Chem. **62,** 507 (2011).

[31] M. Kowalewski, B. P. Fingerhut, K. E. Dorfman, K. Bennett, and S. Mukamel, Simulating coherent multidimensional spectroscopy of nonadiabatic molecular processes: From the infrared to the x-ray regime, Chem. Rev. **117,** 12165 (2017).

[32] U. Bergmann, J. Kern, R. W. Schoenlein, P. Wernet, V. K. Yachandra, and J. Yano, Using x-ray free-electron lasers for spectroscopy of molecular catalysts and metalloenzymes, Nat. Rev. Phys. **3,** 264 (2021).

[33] J. P. Marangos, Accessing the quantum spatial and temporal scales with XFELs, Nat. Rev. Phys. **2,** 332 (2020).

[34] Y. Zhang, T. Kroll, C. Weninger, Y. Michine, F. D. Fuller, D. Zhu, R. Alonso-Mori, D. Sokaras, A. Lutman, A. Halavanau *et al.*, Generation of intense phase-stable femtosecond hard x-ray pulse pairs, arXiv:2110.08262.

[35] J. Qiang, LCLS-II-HE impact tracking, Lawrence Berkeley National Laboratory, Technical Report LCLS-II-HE-TN-20-06, 2019.

[36] H.-D. Nuhn, LCLS-II undulator system physics requirements document, SLAC National Accelerator Laboratory, CA, Technical Report LCLSII-3.2-PR-0038-R2, 2017.

[37] M. Leitner, D. Arbelaez, A. Band, D. Bianculli, A. Brown, J. Corlett, A. DeMello *et al.*, Hard X-ray and soft X-ray undulator segments for the linear coherent light source upgrade (LCLS-II) project, in *Proceedings of 8th International Particle Accelerator Conference (IPAC'17)* (2017), pp. 1605–1608.

[38] Z. Qu, Y. Ma, G. Zhou, and J. Wu, Dynamic pulse-to-pulse thermal load effects in pulse-train-mode self-seeded x-ray free-electron laser, J. Synchrotron Radiat. **27,** 1725 (2020).

[39] Z. Qu, Y. Ma, G. Zhou, and J. Wu, Analytical model for monochromator performance characterizations under thermal load, Opt. Express **28,** 30075 (2020).

[40] J. Wu, B. Yang *et al.*, Thermal stress analysis of a thin diamond crystal under repeated free electron laser heat load, in *Proceedings of the 38th International Free Electron Laser Conference(FEL'17), Santa Fe, NM, 2017* (JACOW, Geneva, Switzerland, 2017), pp. 539–542.

[41] M. Xie, Exact and variational solutions of 3D eigenmodes in high gain FELs, Nucl. Instrum. Methods Phys. Res., Sect. A **445,** 59 (2000).

[42] K. Flottmann, S. Lidia, and P. Piot, Recent improvements to the ASTRA particle tracking code, Lawrence Berkeley National Laboratory (LBNL), Berkeley, CA, Technical Report LBNL-52933, 2003.

[43] M. Borland, Elegant: A flexible SDDS-compliant code for accelerator simulation, Argonne National Laboratory, IL, Technical Report LS-287, 2000.

[44] S. Reiche, Genesis 1.3: A fully 3d time-dependent FEL simulation code, Nucl. Instrum. Methods Phys. Res., Sect. A **429,** 243 (1999).

[45] P. Emma, LCLS-II linac requirements physics requirement document, SLAC National Accelerator Laboratory, CA, Technical Report, 2021.

[46] . B. Schroeder, C. Pellegrini, S. Reiche, J. Arthur, and P. Emma, Chirped-beam two-stage free-electron laser for high-power femtosecond x-ray pulse generation, J. Opt. Soc. Am. B **19,** 1782 (2002).

[47] C. Emma, C. Pellegrini, Y. Ding, G. Marcus, A. Lutman, Z. Huang, and A. Marinelli, Femtosecond x-ray pulse generation with an energy chirped electron beam, *Proceedings of the 15th International Free Electron Laser Conference, Daejeon, Korea* (2015)

[48] Y. Nosochkov, Tuning of r56 in the LCLS-II, SLAC National Accelerator Laboratory, CA, Technical Report LCLS-II-TN-21-10, 2021.

[49] E. Roussel, E. Ferrari, E. Allaria, G. Penco, S. Di Mitri, M. Veronese, M. Danailov, D. Gauthier, and L. Gian-nessi, Multicolor High-Gain Free-Electron Laser Driven by Seeded Microbunching Instability, Phys. Rev. Lett. **115,** 214801 (2015).